Common-Resolution Convolution Kernels for Space- and Ground-Based Telescopes

G. ANIANO,[1] B. T. DRAINE,[1] K. D. GORDON,[2] AND K. SANDSTROM[3]

ABSTRACT. Multiwavelength study of extended astronomical objects requires combining images from instruments with differing point-spread functions (PSFs). We describe the construction of convolution kernels that allow one to generate (multiwavelength) images with a common PSF, thus preserving the colors of the astronomical sources. We generate convolution kernels for the cameras of *Spitzer*, *Herschel Space Observatory*, *Galaxy Evolution Explorer* (*GALEX*), Wide-field Infrared Survey Explorer (WISE), ground-based optical telescopes (Moffat functions and sum of Gaussians), and Gaussian PSFs. Kernels for other telescopes including *IRAS*, *AKARI*, and *Planck*, are currently being constructed. These kernels allow the study of the spectral energy distribution (SED) of extended objects, preserving the characteristic SED in each pixel. The convolution kernels and the IDL packages used to construct and use them are made publicly available.

Online material: color figures

1. INTRODUCTION

Spectral energy distribution studies of astronomical objects provide insight into the ongoing physical processes. In order to achieve a wide range of wavelengths, it is often necessary to combine observations from cameras with very different point-spread functions (PSFs), in some cases with full width at half-maximum (FWHM) differing by factors of 100. Direct comparison (e.g., ratios) of images with structures on multiple angular/spatial scales obtained with different PSFs can result in unphysical intensity ratios (i.e., colors). To preserve colors, intensity ratios should be calculated from images with a common PSF. We therefore require convolution kernels that will transform the images taken with several instruments into a common PSF, so we can generate image cubes (i.e., a collection of images expressed in the same sky coordinates grid) in which each pixel corresponds to the same sky region for all the cameras used.

By "camera" we refer to the combination of telescope optics and physical detector, including the effect of atmospheric "seeing" if applicable. The PSF $\Psi_j(x, y, x', y')$ of a camera j gives the measured intensity at (x, y) produced by a point source with unit flux at the point (x', y'), where we use the Cartesian coordinates (x, y) to denote positions in a small region of the sky. With this definition, the PSF has normalization

$$\iint \Psi_j(x, y, x', y') dx dy = 1, \qquad (1)$$

for any source position (x', y').

It is often possible to approximate the PSF (denoted as Ψ from now on) as constant across the useful field of view of the camera, so $\Psi_j(x, y, x', y') = \Psi_j(x - x', y - y')$. The observed image $I_j(x, y)$ will then be the convolution of the source $S(x, y)$ with the PSF Ψ:

$$I_j(x, y) = \iint S(x', y') \Psi_j(x - x', y - y') dx' dy'$$
$$= (S \star \Psi_j)(x, y). \qquad (2)$$

Clearly, given two cameras A and B, with (different) PSFs Ψ_A and Ψ_B, the images obtained of an astronomical object will be different, even if the spectral response of the cameras were identical. A convolution kernel is a tool that transforms the image observed by one camera into an image corresponding to the PSF of another camera.

The convolution kernel $K\{A \Rightarrow B\}$ from camera A to camera B should satisfy

$$I_B(x, y) = \iint I_A(x', y') K\{A \Rightarrow B\}(x - x', y - y') dx' dy'$$
$$\equiv (I_A \star K\{A \Rightarrow B\})(x, y), \qquad (3)$$

where I_A and I_B are the observed images by the cameras A and B, respectively.

The actual PSF of an instrument will show variations with the source color, variations along the field of view, changes over time, and deviations from rotational symmetry. Full 2D characterization of a PSF is extremely challenging, and its extended wings are often not well determined. To take into account

[1] Princeton University Observatory, Peyton Hall, Princeton, NJ 08544; ganiano@astro.princeton.edu.
[2] SpaceTelescope Science Institute, 3700 San Martin Drive, Baltimore, MD 21218.
[3] Max-Planck Institut fur Astronomie, D-69117 Heidelberg, Germany.

deviations of PSFs from rotational symmetry would require separate kernels $K\{A \Rightarrow B\}(\gamma)$ for each relative orientation γ of cameras A and B. In the present study, the actual PSFs are close enough of having rotational symmetry that such additional complication is not justified (see § 3 for a detailed study). The current work assumes that Ψ_A and Ψ_B can be approximated by rotationally symmetric functions.

Using a different technique, Alard & Lupton (1998) presented a method for finding optimal kernels to convolve (to a common resolution) images of a sky region taken with a single camera under different seeing conditions. Using techniques similar to those used here, Gordon et al. (2008) created kernels for the Infrared Array Camera (IRAC) and Multiband Imaging Photometer for Spitzer (MIPS) cameras of *Spitzer*, and Sandstrom et al. (2009) created kernels for the Infrared Spectrograph (IRS) of *Spitzer*. In the present work, we use the latest characterization of the PSFs of the cameras on *Spitzer* (IRAC and MIPS), *Herschel Space Observatory* (Photocamera Array Camera and Spectrometer for *Herschel* [PACS] and Spectral and Photometric Imaging Receiver for *Herschel* [SPIRE]), *Galaxy Evolution Explorer* (*GALEX*) (FUV, NUV), and the Wide-field Infrared Survey Explorer (WISE) (W1–W4). Additional PSFs (including those characterizing the IRS spectrograph on board *Spitzer*; the PACS spectrographs on board the *Herschel Space Observatory*; and all-sky images produced by *IRAS*, *AKARI*, and *Planck*) are currently being constructed and will be added to the kernel library. We also include a family of analytical PSF profiles that are commonly used to model the PSFs for ground-based telescopes. We construct the set of kernels to transform from different instrumental PSFs into Gaussian PSFs, another form that is widely used. We find an optimal Gaussian PSF for each camera: i.e., a Gaussian PSF that is sharp enough to capture the angular resolution of the camera and wide enough to be robust against image artifacts.

Additional image processing (i.e., co-adding images[4]) or different data reduction schemes (i.e., the Scanamorphos pipeline [Roussel 2011] for the *Herschel* images) will alter the PSF, and thus new kernels should be constructed using the effective PSF.

This article is organized as follows. In § 2 we describe the generation of convolution kernels, in § 3 we describe the PSF used, and in § 4 we describe the kernel construction strategy. The performance of the kernels is examined in § 5, and in § 6 we describe a set of Gaussian kernels that are compatible with the different instruments. In § 7 we describe the kernel usage and show their performance on NGC 1097, and we summarize in § 8.

All the kernels, IDL routines to use the kernels, and IDL routines to make new kernels, along with detailed analysis of the generated kernels, are publicly available.[5]

2. CONVOLUTION KERNELS

Given two cameras A and B, with PSFs Ψ_A and Ψ_B, we seek $K\{A \Rightarrow B\}$ that fulfills equation (3) for any astronomical source. Thus,

$$(S \star \Psi_B) = I_B = (I_A \star K\{A \Rightarrow B\}) = (S \star \Psi_A \star K\{A \Rightarrow B\}) \tag{4}$$

for any astronomical source S, so the convolution kernel must satisfy

$$\Psi_B = (\Psi_A \star K\{A \Rightarrow B\}). \tag{5}$$

With the normalization condition given by equation (1), the kernel must have

$$\iint K\{A \Rightarrow B\}(x, y)dxdy = 1. \tag{6}$$

We can easily invert equation (5) in Fourier space; taking the two-dimensional Fourier transform (FT) of equation (5)[6] we obtain

$$\begin{aligned} \mathrm{FT}(\Psi_B) &= \mathrm{FT}(\Psi_A \star K\{A \Rightarrow B\}) \\ &= \mathrm{FT}(\Psi_A) \times \mathrm{FT}(K\{A \Rightarrow B\}). \end{aligned} \tag{7}$$

This can be inverted to obtain

$$K\{A \Rightarrow B\} = \mathrm{FT}^{-1}\left(\mathrm{FT}(\Psi_B) \times \frac{1}{\mathrm{FT}(\Psi_A)} \right), \tag{8}$$

where FT and FT^{-1} stand for the Fourier transform and its inverse transformation, respectively.

Equation (8) provides a condition for the existence of such a kernel and a practical way of computing it. We can see that a condition for the existence of a kernel is that the Fourier components for which $\mathrm{FT}(\Psi_A) = 0$ should satisfy $\mathrm{FT}(\Psi_B) = 0$. Informally speaking, this means that the PSF of camera A must be narrower than the PSF of camera B.

For each camera A, we identify a high-frequency cutoff $k_{H,A}$ as the highest spatial frequency for which $\mathrm{FT}(\Psi_A)$ is appreciable by setting

$$\mathrm{FT}(\Psi_A)(k_{H,A}) = 5 \times 10^{-3} \times \max[\mathrm{FT}(\Psi_A)]. \tag{9}$$

The cutoff frequency $k_{H,A}$ can be normalized as $k_{H,A} = \kappa_A \times 2\pi/\mathrm{FWHM}_A$. The values of κ_A are in the range of 1.08–1.46 and are given in Table 1.

---

[4]For example, for 2MASS co-added images the images undergo an additional smearing with a kernel whose size corresponds to a detector pixel.

[5]See http://www.astro.princeton.edu/~draine/Kernels.html. Kernels for additional cameras and updates will be included when new PSF characterizations become available.

[6]Computing the two-dimensional Fourier transform of rotationally symmetric functions is mathematically equivalent to making a decomposition in the one-parameter family of Bessel functions. However, the existence of the fast Fourier transform (FFT) algorithm makes it numerically more efficient to perform the decomposition in the family of Fourier modes.

TABLE 1
BASIC INSTRUMENT INFORMATION

Camera	Rayleigh diff. limit [a] (")	Measured FWHM (")	99% of energy radius (")	κ [b]	Asymmetry g [c]
IRAC 3.6 μm	1.04	1.90	62.52	1.29	0.16
IRAC 4.5 μm	1.31	1.81	64.46	1.26	0.17
IRAC 5.8 μm	1.68	2.11	133.55	1.20	0.19
IRAC 8.0 μm	2.30	2.82	114.20	1.19	0.18
MIPS 24 μm	6.93	6.43	224.53	1.05	0.08
MIPS 70 μm	20.90	18.74	461.44	1.12	0.05
MIPS 160 μm	45.62	38.78	678.77	1.10	0.05
PACS 70 μm	5.11	5.67	249.81	1.23	0.20
PACS 100 μm	7.28	7.04	350.63	1.19	0.20
PACS 160 μm	11.70	11.18	417.36	1.21	0.20
SPIRE 250 μm	17.93	18.15	205.07	1.16	0.19
SPIRE 350 μm	25.16	24.88	192.47	1.15	0.18
SPIRE 500 μm	36.22	36.09	198.43	1.16	0.19
GALEX FUV	0.08	4.48	50.28	1.26	0.07
GALEX NUV	0.11	5.05	39.56	1.32	0.05
WISE 3.35 μm	2.11	5.79	19.10	1.20	0.17
WISE 4.60 μm	2.89	6.37	19.08	1.33	0.13
WISE 11.56 μm	7.27	6.60	19.56	1.23	0.12
WISE 22.1 μm	13.90	11.89	35.15	1.05	0.07
Gauss 12″	...	12.00	15.41	1.33	0.0
Gauss 20″	...	20.00	25.68	1.33	0.0
Gauss 23″	...	23.00	29.53	1.33	0.0
Gauss 28″	...	28.00	35.95	1.33	0.0
Gauss 40″	...	40.00	51.33	1.33	0.0
Gauss 50″	...	50.00	64.05	1.33	0.0
BiGauss 0.5″	...	0.50	0.90	1.37	0.0
BiGauss 1.0″	...	1.00	1.79	1.37	0.0
BiGauss 1.5″	...	1.50	2.69	1.37	0.0
BiGauss 2.0″	...	2.00	3.57	1.37	0.0
BiGauss 2.5″	...	2.50	4.44	1.37	0.0
Moffat 0.5″	...	0.50	1.39	1.46	0.0
Moffat 1.0″	...	1.00	2.77	1.46	0.0
Moffat 1.5″	...	1.50	4.12	1.46	0.0
Moffat 2.0″	...	2.00	5.45	1.46	0.0
Moffat 2.5″	...	2.50	6.74	1.46	0.0

[a] We take the Rayleigh diffraction limit as $1.22 \times [\text{central}\lambda]/[\text{telescope diameter}]$.
[b] We define κ as $(k_H \times \text{FWHM}_A)/(2\pi)$, where k_H is the high-frequency cutoff (see text for details).
[c] The parameter g is a measure of the departure of a PSF from rotational symmetry (see eq. [12]).

Equation (8) also provides insight of a possible problem in computing kernels. PSF Fourier transforms do not have significant power at (spatial) frequencies above the $2\pi/\text{FWHM}$. The high-frequency components of the FT will be small, introducing large uncertainties when inverted.

A possible way of avoiding problems in the high-frequency components of the kernel is to introduce a filter f_A in the kernel construction:

$$K\{A \Rightarrow B\} = \text{FT}^{-1}\left(\text{FT}(\Psi_B) \times \frac{1}{\text{FT}(\Psi_A)} \times f_A\right), \quad (10)$$

where f_A is a suitable low-pass filter. Because this differs from equation (8), it is clear that a kernel satisfying equation (10) will, in general, not be an exact solution to equation (8).

However, we can expect that if the filter f_A does not remove significant power from the high-frequency components of either $\text{FT}(\Psi_A)$ or $\text{FT}(\Psi_B)$, then the kernel computed will be a good approximate solution to equation (8).

We use a filter f_A of the form

$$f_A(k) = \begin{cases} 1 & \text{for } k \leq k_{L,A} \\ \frac{1}{2} \times \left[1 + \cos\left(\pi \times \frac{k - k_{L,A}}{k_{H,A} - k_{L,A}}\right)\right] & \text{for } k_{L,A} \leq k \leq k_{H,A}, \\ 0 & \text{for } k_{H,A} \leq k \end{cases}$$

$$(11)$$

where we set $k_{L,A} = 0.7 \times k_{H,A}$. Note that the cutoff frequency of our filter f_A depends only on camera A, since small values of $\text{FT}(\Psi_B)$ have no negative impact in the kernel construction. In

principle, any smoothly varying function that is close to 1 in the low-frequency range and goes to zero in frequencies larger than $k_{H,A}$ should work as well. We have experimented using several smoothing functions and find that the particular form of $f_A(k)$ given by equation (11), with these particular choices of $k_{L,A}$ and $k_{H,A}$, gives excellent results. More details of the smoothing function effects can be found in § 5.

If the cutoff frequencies associated with cameras A and B are such that $k_{H,B} \leq k_{H,A} \times 0.7$, then the filter f_A has little effect and the resulting kernel from equation (10) will satisfy equation (3) to a very good approximation. In the regime $k_{H,A} \times 0.7 \leq k_{H,B} \leq k_{H,A}$ the kernel $K\{A \Rightarrow B\}$ will depend on the exact form of the filter f_A used. Most of the kernels in this regime have good performance; the performance of such "filtered" kernels will be evaluated in § 5. A limiting case is a kernel $K\{A \Rightarrow A\}$ that transforms a PSF into itself; it is the Fourier transform of the filter f_A.

In the cases of $k_{H,A} < k_{H,B}$ (convolving into narrower PSFs), use of the filter f_A allows one to compute convolution kernels, but their performance can be poor. This will be further discussed subsequently

3. INSTRUMENTAL POINT-SPREAD FUNCTIONS

We generate appropriate kernels for the measured PSFs of the cameras on *Spitzer*, *Herschel*, *GALEX*, and WISE and for certain analytical PSFs that are used in the literature:

IRAC.—The Infrared Array Camera (Fazio et al. 2004) has four infrared bands, centered at 3.6 μm, 5.0 μm, 5.8 μm, and 8.0 μm. We use the in-flight extended point response functions (PRFs).[7] The core portion of the PSF was made with 300 observations of a calibration, with different exposure time, combined into a high dynamic range image. Observations of the stars Vega, ϵ Eridani, Fomalhaut, ϵ Indi, and Sirius were used in the construction of the extended wings of the PSF.[8]

MIPS.—The Multiband Imaging Photometer for *Spitzer* (Rieke et al. 2004) has three photometric infrared bands, centered at 24 μm, 70 μm, and 160 μm. Following Engelbracht et al. (2007), Gordon et al. (2007), and Stansberry et al. (2007), we generate theoretical PSFs for the MIPS cameras, assuming a blackbody source at $T = 25$ K. The PSFs are generated using the software STinyTim[9] in a 0.5″ grid, and they are smoothed with a square kernel with sides of 4.5″, 13.5″, and 25.5″ for the bands at 70 μm, 100 μm, and 160 μm respectively. The smoothing sizes correspond to 1.6, 1.35, and 1.8 times the camera detector pixel size, and they should cause the core of the

theoretical PSF to be in close agreement with the calibration point-source images.

PACS.—The Photocamera Array Camera and Spectrometer for *Herschel* (Poglitsch et al. 2010) has three photometric infrared bands, centered at 70 μm, 100 μm, and 160 μm. We use the in-flight PSF (Geis & Lutz 2010; Lutz 2010; Müller 2010); the core was defined by observations of the star α Tau and the asteroid Vesta, with extended wings reconstructed from (saturated) observations of Mars, Neptune, IK Tau, and the Red Rectangle. The azimuthally averaged encircled energy fraction of the PSFs out to 1000″ were obtained from the HCSS/HIPE software.

SPIRE.—The Spectral and Photometric Imaging Receiver for *Herschel* (Griffin et al. 2010) has three photometric far-infrared bands, centered at 250 μm, 350 μm, and 500 μm.[10]

GALEX.—The Galaxy Evolution Explorer (Martin et al. 2005) has two ultraviolet bands, FUV (1350–1750 Å) and NUV (1750–2800 Å).[11]

WISE.—The Wide-field Infrared Survey Explorer (Wright et al. 2010) has four photometric infrared bands, centered at 3.4 μm, 4.6 μm, 12 μm, and 22 μm. The PSF shape varies significantly over the focal plane due to distortion from the telescope optics; so a library of PSFs corresponding to a 9×9 grid of locations on the focal plane was determined. For each camera, we average the 81 different PSFs to generate a single PSF per camera.

As a way of measuring the departure of a PSF Ψ_j from rotational symmetry, we define an asymmetry parameter:

$$g_j \equiv \iint |\Psi_j - C[\Psi_j]| dx dy, \qquad (12)$$

where $C[\Psi_j]$ is the azimuthally averaged version of Ψ_j (i.e., $C[\Psi_j]$ is a PSF with rotational symmetry and the same radial profile as Ψ_j). The PSFs used have $g \lesssim 0.2$.

In Table 1 we have a summary of the properties of the different PSFs: the camera Rayleigh diffraction angle, the PSF FWHM, the radius containing 99% of the PSF energy, the (normalized) high-frequency cutoff κ_A used in the filter f_A, and the anisotropy parameter g. The PSF radial profiles [out to $\Psi(\theta) \approx 10^{-5}\Psi(0)$] and enclosed power are plotted in Figures 1 and 2.

For each PSF the radii containing 25%, 50%, 65%, 80%, 90%, 95%, 98%, 99%, 99.5%, and 99.9% of the total power are given in Table 2. Table 3 gives the enclosed power for selected radii.

For convenience, we add several families of PSFs that are often used for ground-based optical and radio telescopes. For

---

[7] In the current work we always use the full response of the optical systems including the camera effects, and for simplicity we will not make any further distinction between PSFs and PRFs.

[8] The PSFs are available at http://ssc.spitzer.caltech.edu/.

[9] STinyTim is available at http://irsa.ipac.caltech.edu/data/SPITZER/docs/data analysistools/tools/contributed/general/stinytim/.

[10] We use the in-flight 1.0″ PSF maps from ftp://ftp.sciops.esa.int/pub/hsc-calibration/SPIRE/.

[11] In-flight PSFs are available at http://www.galex.caltech.edu/researcher/techdoc-ch5.html.
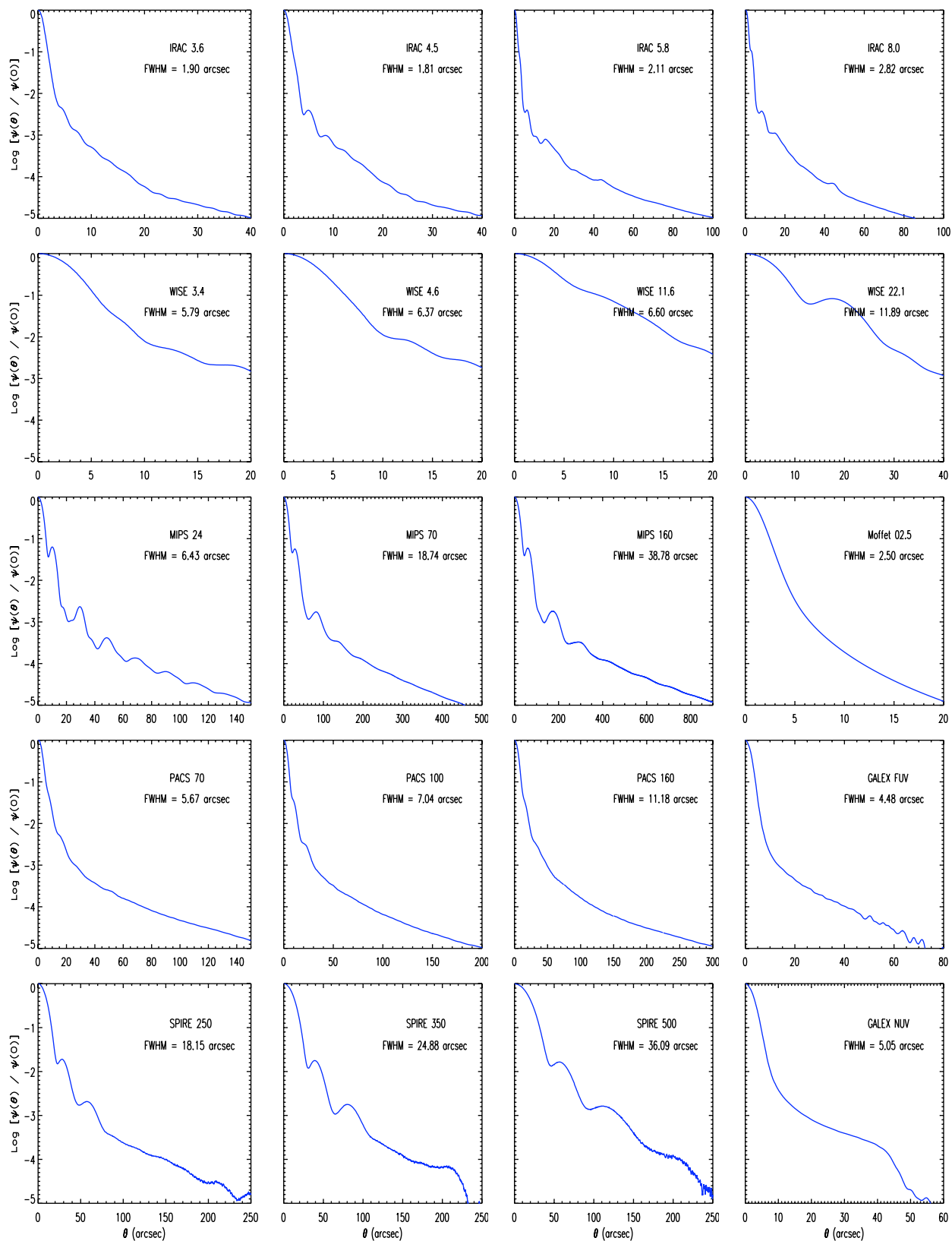
FIG. 1.—PSF radial profiles for the 20 cameras considered here (see text). All PSFs are shown out to $\Psi(\theta) \approx 10^{-5}\Psi(0)$, with the exception of WISE (W1–W4), for which we have data only down to $\approx 0.002\Psi(0)$. See the electronic edition of the *PASP* for a color version of this figure.
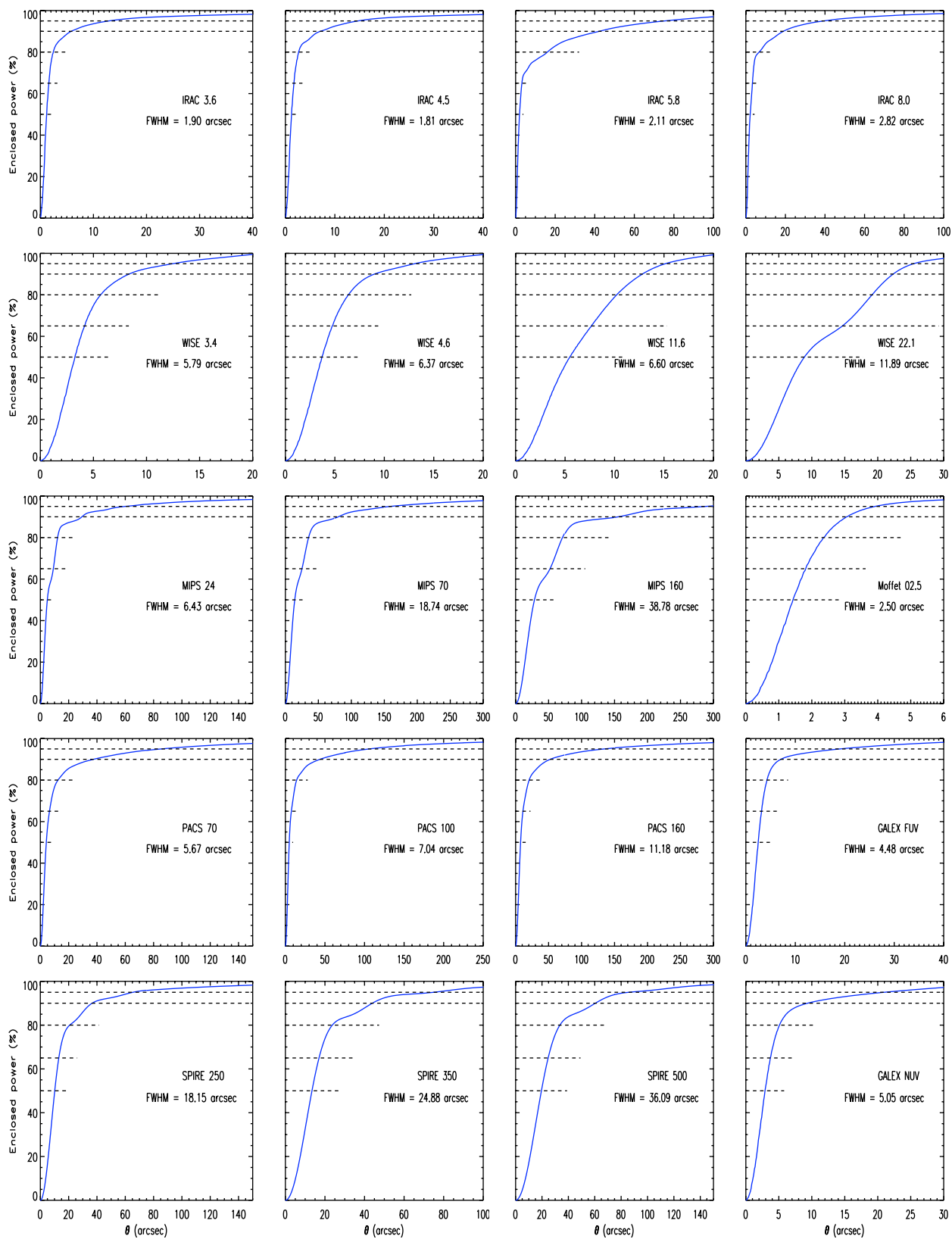
Fig. 2.—Fraction of the power enclosed by a circle of radius θ for the 20 cameras considered (see text). See the electronic edition of the *PASP* for a color version of this figure.

TABLE 2
ENCLOSED ENERGY PERCENT (%) IN SELECTED CIRCULAR APERTURES

Camera	Radii (") 2.5	5	7.5	10	12.5	15	17.5	20	25	30	40	50	60	90	120
IRAC 3.6 μm	80.7	88.7	91.8	93.6	94.8	95.7	96.3	96.7	97.2	97.6	98.2	98.6	98.9	99.5	99.8
IRAC 4.5 μm	78.1	86.7	90.3	92.5	94.0	95.1	95.9	96.5	97.1	97.5	98.1	98.6	98.9	99.5	99.8
IRAC 5.8 μm	57.6	70.5	74.2	76.0	77.6	79.2	81.2	82.9	85.4	87.0	89.5	91.7	93.2	96.3	98.3
IRAC 8.0 μm	53.9	78.0	80.8	84.0	85.9	87.6	89.3	90.5	92.3	93.5	95.1	96.2	96.9	98.3	99.2
MIPS 24 μm	21.6	50.5	59.4	69.1	81.2	85.5	86.5	87.2	88.3	90.4	92.7	94.0	95.0	96.7	97.8
MIPS 70 μm	3.00	11.2	22.5	34.2	44.3	51.5	56.1	59.1	64.4	71.8	83.9	87.1	88.0	91.3	93.4
MIPS 160 μm	0.73	2.88	6.32	10.8	16.1	21.8	27.8	33.5	43.8	51.3	58.9	63.4	70.4	86.9	88.7
PACS 70 μm	26.8	56.8	69.3	76.6	80.0	82.2	84.1	85.6	87.3	88.6	90.4	91.8	92.9	95.3	96.7
PACS 100 μm	20.4	51.3	65.0	71.8	77.6	80.8	82.5	83.7	86.2	87.7	89.5	90.8	91.9	94.2	95.6
PACS 160 μm	8.89	29.3	49.0	61.2	67.8	72.3	76.2	79.3	82.8	84.7	87.6	89.5	90.8	93.1	94.5
SPIRE 250 μm	4.39	16.3	32.4	48.9	62.6	71.8	77.0	79.5	82.2	85.9	91.0	92.5	94.0	96.5	97.5
SPIRE 350 μm	2.48	9.56	20.1	32.7	45.6	57.2	66.9	73.9	81.2	83.5	87.8	92.5	94.0	96.6	97.9
SPIRE 500 μm	1.17	4.62	10.1	17.2	25.5	34.3	43.2	51.7	66.0	75.8	83.9	86.5	89.9	95.2	97.1
GALEX FUV	50.2	84.9	90.5	92.2	93.2	94.0	94.6	95.2	96.2	97.0	98.2	99.0	99.5	100	100
GALEX NUV	40.7	79.3	88.1	90.5	91.9	93.0	93.9	94.7	96.1	97.2	99.1	99.8	99.9	100	100
WISE 3.35 μm	34.5	74.8	87.7	92.6	95.0	96.9	98.2	99.4	100	100	100	100	100	100	100
WISE 4.60 μm	28.4	68.0	85.9	91.5	94.4	96.7	98.2	99.4	100	100	100	100	100	100	100
WISE 11.56 μm	18.6	46.1	64.0	78.9	89.1	94.8	97.5	99.3	100	100	100	100	100	100	100
WISE 22.1 μm	7.36	24.9	42.8	54.3	60.4	66.0	74.0	83.1	94.5	97.6	99.7	100	100	100	100
Gauss 12″	11.3	38.2	66.2	85.5	95.1	98.7	99.8	100	100	100	100	100	100	100	100
Gauss 20″	4.24	15.9	32.3	50.0	66.2	79.0	88.1	93.8	98.7	99.8	100	100	100	100	100
Gauss 23″	3.22	12.3	25.5	40.8	55.9	69.3	79.9	87.7	96.3	99.1	100	100	100	100	100
Gauss 28″	2.18	8.46	18.0	29.8	42.5	54.9	66.2	75.7	89.1	95.9	99.7	100	100	100	100
Gauss 40″	1.08	4.24	9.29	15.9	23.7	32.3	41.2	50.0	66.2	79.0	93.8	98.7	99.8	100	100
Gauss 50″	0.69	2.73	6.05	10.5	15.9	22.1	28.8	35.8	50.0	63.2	83.1	93.8	98.2	100	100
BiGauss 0.5″	100	100	100	100	100	100	100	100	100	100	100	100	100	100	100
BiGauss 1.0″	99.9	100	100	100	100	100	100	100	100	100	100	100	100	100	100
BiGauss 1.5″	98.6	100	100	100	100	100	100	100	100	100	100	100	100	100	100
BiGauss 2.0″	95.7	99.9	100	100	100	100	100	100	100	100	100	100	100	100	100
BiGauss 2.5″	89.9	99.5	100	100	100	100	100	100	100	100	100	100	100	100	100
Moffat 0.5″	100	100	100	100	100	100	100	100	100	100	100	100	100	100	100
Moffat 1.0″	98.7	100	100	100	100	100	100	100	100	100	100	100	100	100	100
Moffat 1.5″	96.1	99.5	100	100	100	100	100	100	100	100	100	100	100	100	100
Moffat 2.0″	90.9	98.7	99.7	100	100	100	100	100	100	100	100	100	100	100	100
Moffat 2.5″	83.0	97.7	99.3	99.8	100	100	100	100	100	100	100	100	100	100	100

each analytical profile, we generate the kernels for a range of FWHM values. We consider the following analytical profiles:

Gaussians.—We use a Gaussian PSF of the form

$$\Psi(\theta) = \frac{1}{2\pi\sigma^2} \exp\left(\frac{-\theta^2}{2\sigma^2}\right), \tag{13}$$

where the FWHM $= 2 \times \sigma\sqrt{2\ln 2}$. We generate kernels with $5'' <$ FWHM $< 65''$.

Optical (SDSS).—In the SDSS survey, it is found that a good approximation to the telescope PSF is given by the sum of two Gaussians. The two components have relative weights of 0.9 and 0.1, and the FWHM of the second component is twice that of the first. We use a family of PSFs of the form

$$\Psi(\theta) = 0.9\frac{1}{2\pi\sigma^2}\exp\left(\frac{-\theta^2}{2\sigma^2}\right) + 0.1\frac{1}{2\pi(2\sigma)^2}\exp\left(\frac{-\theta^2}{2(2\sigma)^2}\right). \tag{14}$$

where the FWHM $= 1.01354 \times 2 \times \sigma\sqrt{2\ln 2}$. We generate kernels with FWHM $= 0.5, 1.0, 1.5, 2.0,$ and $2.5''$.

Optical (General).—Moffat (1969) proposed PSFs of the form

$$M_\beta(\theta) = \frac{(\beta-1)(2^{1/\beta}-1)}{\pi\theta_0^2}\left[1 + (2^{1/\beta}-1)\left(\frac{r}{\theta_0}\right)^2\right]^{-\beta}, \tag{15}$$

where β is a parameter, and FWHM $= 2\theta_0$, Following Racine (1996) we use PSFs of the form

$$\Psi(r) = 0.8 \times M_7(\theta) + 0.2 \times M_2(\theta), \tag{16}$$

TABLE 3
RADII (") ENCLOSING SELECTED PERCENTS OF TOTAL POWER

Camera	Percent (%)									
	25	50	65	80	90	95	98	99	99.5	99.9
IRAC 3.6 μm	0.74	1.19	1.60	2.44	5.83	12.9	36.0	62.5	88.1	132
IRAC 4.5 μm	0.75	1.24	1.73	2.68	7.06	14.7	37.9	64.5	90.8	134
IRAC 5.8 μm	0.99	1.97	3.17	16.0	42.3	75.3	114	134	145	154
IRAC 8.0 μm	1.16	2.21	3.32	6.70	18.9	39.5	82.9	114	134	152
MIPS 24 μm	2.73	4.93	9.18	12.2	29.4	60.4	130	225	368	738
MIPS 70 μm	8.02	14.4	25.5	35.6	80.2	158	318	461	628	894
MIPS 160 μm	16.3	29.0	52.8	71.9	155	287	518	679	802	950
PACS 70 μm	2.41	4.23	6.47	12.5	37.5	85.3	165	250	378	712
PACS 100 μm	2.83	4.87	7.50	14.1	43.5	105	227	351	477	711
PACS 160 μm	4.50	7.66	11.3	20.8	53.3	133	294	417	524	712
SPIRE 250 μm	6.39	10.2	13.1	20.8	36.6	66.1	138	205	382	488
SPIRE 350 μm	8.49	13.4	17.0	23.7	43.9	75.0	122	192	397	499
SPIRE 500 μm	12.4	19.5	24.6	33.5	60.3	85.9	137	198	411	511
GALEX FUV	1.59	2.49	3.17	4.27	7.05	19.0	38.3	50.3	59.7	75.1
GALEX NUV	1.82	2.90	3.71	5.08	9.34	20.9	33.9	39.6	43.4	58.7
WISE 3.35 μm	2.03	3.26	4.17	5.67	8.36	12.5	17.2	19.1	20.2	21.4
WISE 4.60 μm	2.29	3.69	4.75	6.36	9.00	13.0	17.2	19.1	20.2	21.4
WISE 11.56 μm	3.02	5.48	7.66	10.2	12.8	15.1	18.1	19.6	20.5	21.5
WISE 22.1 μm	5.01	8.87	14.6	19.1	22.3	25.4	31.2	35.1	38.5	42.1
Gauss 12″	3.86	6.00	7.38	9.14	10.9	12.5	14.2	15.4	16.5	18.5
Gauss 20″	6.44	10.00	12.3	15.2	18.2	20.8	23.7	25.7	27.5	30.9
Gauss 23″	7.41	11.5	14.1	17.5	20.9	23.9	27.3	29.5	31.6	35.5
Gauss 28″	9.02	14.0	17.2	21.3	25.5	29.1	33.2	36.0	38.5	43.2
Gauss 40″	12.9	20.0	24.6	30.5	36.4	41.5	47.4	51.3	54.9	61.5
Gauss 50″	16.1	25.0	30.8	38.1	45.5	51.9	59.2	64.1	68.4	76.3
BiGauss 0.5″	0.17	0.26	0.32	0.41	0.50	0.60	0.76	0.90	1.02	1.25
BiGauss 1.0″	0.33	0.52	0.64	0.81	1.00	1.20	1.53	1.79	2.04	2.50
BiGauss 1.5″	0.50	0.78	0.97	1.22	1.50	1.80	2.29	2.69	3.05	3.71
BiGauss 2.0″	0.66	1.04	1.29	1.62	2.00	2.40	3.04	3.57	4.04	4.86
BiGauss 2.5″	0.83	1.30	1.61	2.03	2.50	3.00	3.79	4.44	5.01	5.96
Moffat 0.5″	0.18	0.29	0.36	0.47	0.60	0.76	1.07	1.39	1.72	2.26
Moffat 1.0″	0.36	0.57	0.72	0.94	1.21	1.53	2.14	2.77	3.43	4.50
Moffat 1.5″	0.54	0.86	1.08	1.41	1.81	2.29	3.19	4.12	5.09	6.70
Moffat 2.0″	0.71	1.14	1.44	1.88	2.42	3.05	4.23	5.45	6.69	8.90
Moffat 2.5″	0.89	1.43	1.81	2.34	3.02	3.80	5.27	6.74	8.29	11.1

where the same θ_0 is used in M_7 and M_2. We generate kernels with FWHM = $2\theta_0$ = 0.5, 1.0, 1.5, 2.0, and 2.5″.

4. KERNEL GENERATION

Generation of the convolution kernels was accomplished as follows.

4.1. Input the PSF and Correct for Missing Data

When an input PSF image has missing data pixels (like the current SPIRE PSFs), we iteratively estimate the missing values.

We start by replacing the missing data pixels by a value of 0 in the original image. We compute a smoothed image by convolving it with a (normalized) Gaussian kernel $\propto \exp[-(\theta/2\theta_0)^2]$, with θ_0 equal to 2 pixels. We replace the original image missing data pixels by the value they have in the convolved image (the original data are not altered). We iterate the convolution and replacement steps 5 times. The resulting image has all the missing data points replaced by a smooth interpolation. This technique produces robust results, even if we have missing data in a patch of a few contiguous pixels.

4.2. Resample the PSFs

Each PSF comes in a grid of different pixel size. We transform each PSF into a grid of a common pixel size of 0.20″ using the IDL procedure congrid, using the *cubic convolution* interpolation method with a parameter of −0.5. The 0.20″ pixel size captures all the details on the instrumental and Gaussian PSFs. We also pad with 0 the resulting images into an odd-sized square array if needed.

We use a grid of a common pixel size of 0.10″ to regenerate the kernels from optical PSFs into IRAC cameras.

4.3. Center the PSFs

To determine the image center, we smooth the image with a 5 pixel radius circular kernel and locate the image maximum. In some PSFs the maximum value is achieved over a (small) ring. To avoid possible misidentification of the real image center, we take the centroid of all the pixels that satisfy

$$\frac{\max[\Psi] - \Psi(x,y)}{\max[\Psi]} \leq 5 \times 10^{-4}. \qquad (17)$$

4.4. Circularize the PSFs

In order to make a rotationally symmetric PSF, we average over 2^{14} rotations of the image through angles $\beta_n = n \times 360°/2^{14}$ for $n = 1, 2, 3, ..., 2^{14} = 16,384$, producing a PSF image that is invariant under rotations of any angle that is a multiple of $360°/2^{14} = 0.022°$ (i.e., is as rotationally symmetric as we can numerically expect).

Computing 2^{14} rotations naively would be extremely time-consuming, but the final result can in fact be computed performing only 14 rotations, as follows.

We start by rotating Ψ by an angle $\theta_1 = 360°/2^1 = 180°$, producing an image R_1, and computing their average $\bar{R}_1 = \frac{1}{2} \times [\Psi + R_1]$. Clearly, $\bar{R}_1$ is now invariant under rotations of $\theta_1 = 360°/2^1 = 180°$.

We continue this procedure iteratively. We rotate R_1 by an angle $\theta_2 = 360°/2^2 = 90°$, producing an image R_2, and set $\bar{R}_2 = \frac{1}{2} \times [\bar{R}_1 + \bar{R}_2]$. $\bar{R}_2$ is invariant under rotations of $\theta_1 = 360°/2^1 = 180°$ and $\theta_2 = 360°/2^2 = 90°$; i.e. it is invariant under rotations of any angle that is a multiple of $360°/2^2 = 90°$.

We iterate this procedure 14 times; the last average calculated image $\bar{R}_{14}$ is the desired rotationally symmetric PSF.

We further set to 0 all the pixels that lie outside the largest circle included in the square image, since those regions would correspond to areas with partial image coverage. If there are pixels with (very small) negative values (due to the noise in the original PSFs) we set them to 0.

In order to have a more stable algorithm, the previous rotations are performed in reverse order (i.e., starting with the smallest angles).

All the remaining steps in the kernel construction should preserve the rotational symmetry in the images. A way of estimating the noise induced by some steps (e.g., computing Fourier transform) is to compute the departure from rotational symmetry in the resulting image. Circularizing helps to reduce numerical noise and will be performed after every step that can potentially decrease the image quality. When a circularization is performed to a rotationally symmetric image, the asymmetry parameter g of the resulting image is smaller than 0.0008 (i.e., the circularization procedure itself induces very small departures from rotational symmetry).

4.5. Resize the PSFs

We trim (or pad with 0) all the PSFs into a common grid, to be able to compute all the convolution kernels using only one Fourier transform per PSF. We choose a grid size that is large enough to contain most of the power in each PSF. We also optimize its size to make the FFT algorithm as efficient as possible (minimal sum of prime factors). The adopted grid size is $729'' \times 729''$, giving an image size of 3645×3645 pixels.

4.6. Compute the Fourier Transform of the PSF FT(Ψ)

We use an efficient FFT algorithm. Since the PSFs are invariant under reflections, $\vec{x} \leftrightarrow -\vec{x}$, their Fourier transform should be real. We impose this real condition to reduce the numerical noise introduced by the double-precision FFT algorithm.

4.7. Circularize the FT(Ψ)

Using the procedure as before, we circularize the FT(Ψ). In principle, they should already be rotationally symmetric, but numerical noise in the FFT algorithm makes them slightly non-rotationally symmetric.

4.8. Filter the FT(Ψ)

We filter the highest frequencies in each FT(Ψ). We use a filter ϕ of the form

$$\phi(k) = \begin{cases} 1 & \text{for } k \leq k_\alpha \\ \exp\left[-\left(1.8249 \times \frac{k - k_\alpha}{k_\beta - k_\alpha}\right)^4\right] & \text{for } k_\alpha \leq k \leq k_\beta, \\ 0 & \text{for } k_\beta \leq k \end{cases}$$

$$(18)$$

where we set $k_\alpha = 0.9 \times k_\beta$. The factor 1.8249 is chosen so that $\phi(0.5 \times (k_\beta + k_\alpha)) = 0.5$. For each camera we choose $k_\beta = 4 \times (2\pi/\text{FWHM})$. We tested several filter functions and found that the particular form given by equation (19) provided the best results. Each PSF has structure at spatial wavelengths comparable with the FWHM, so the Fourier components with frequencies much higher than this cannot be important. The Fourier components removed by this filter were mainly introduced by the original image resizing algorithm. In the following discussion, we let $\text{FT}_\phi(\Psi) = \phi \times \text{FT}(\Psi)$.

4.9. Invert the FT(Ψ)

We evaluate $1/\text{FT}_\phi(\Psi)$ at the points where $\text{FT}_\phi(\Psi) \neq 0$. We set $1/\text{FT}_\phi(\Psi) = 0$ at the remaining points (which will be filtered soon).

4.10. Compute the FT of the Filtered Kernel

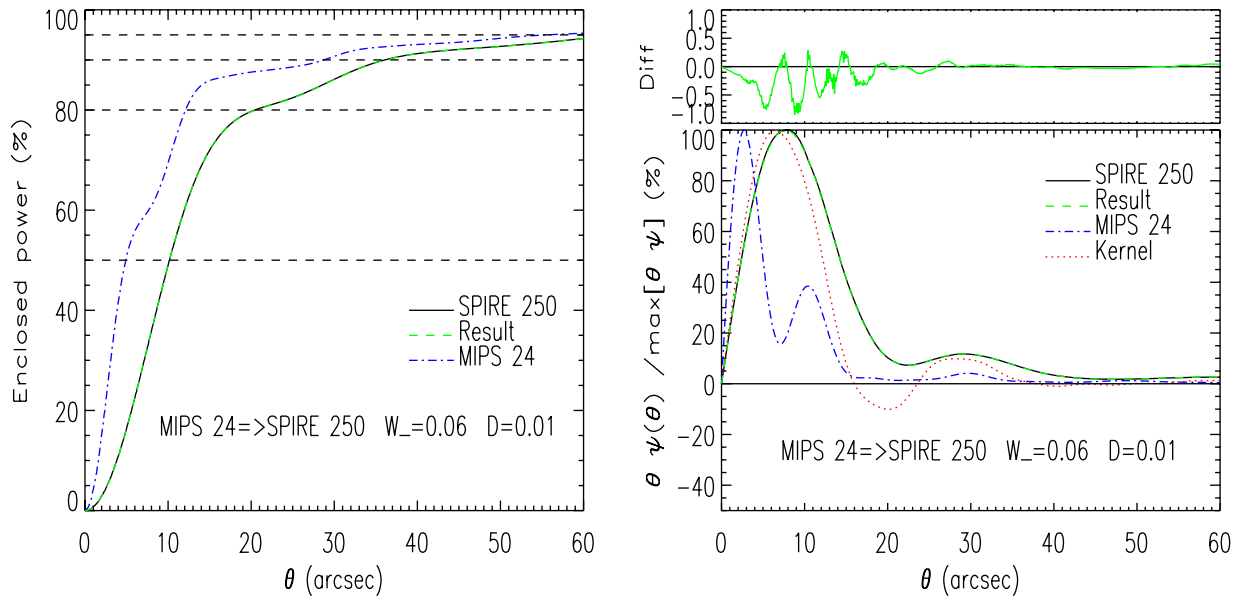We compute the FT of the filtered kernel using the filter f_A from equation (11):

FIG. 3.—Performance of the filtered kernel $K\{\text{M24} \Rightarrow \text{S250}\}$. W_- is the integral of the negative values of the kernel, and D is the integral of the absolute value of the difference between the target PSF and the PSF reproduced by the kernel (see eq. [20]). See the electronic edition of the *PASP* for a color version of this figure.

$$\text{FT}(K\{A \Rightarrow B\}) = \text{FT}_\phi(\Psi_B) \times \frac{f_A}{\text{FT}_\phi(\Psi_A)} \qquad (19)$$

for all the appropriate combinations (A, B).

4.11. Compute the Kernels

We compute the inverse Fourier transform to the previously calculated $\text{FT}(K)$. We again impose the condition that K must be real.

4.12. Circularize the Kernels

Using the procedure as before, we circularize the kernels. Again, they should already be rotationally symmetric. Numerical noise in the inverse FFT algorithm makes them slightly asymmetric, but this is easily corrected.

4.13. Resample the Kernels

All the computed kernels are given in a grid of a common pixel size of 0.20″, but will be needed in grids of different pixel sizes. Again, we resample the kernels using the IDL procedure `congrid`, using the cubic convolution interpolation method with a parameter of -0.5.

4.14. Final Trim of the Kernels

We trim each kernel to a smaller size (to speed up further convolution) such that it contains 99.9% of the total kernel energy. Moreover, we use a square grid with an odd number of pixels so that the kernel peaks in a single central pixel.

4.15. Circularize the Final Kernels

We finish the kernels by circularizing them again, to remove the small noise introduced in the resampling process. All previous calculations were done in double precision to reduce numerical noise.

5. KERNEL PERFORMANCE

For each generated kernel, we compute $\Psi_A \star K\{A \Rightarrow B\}$, the convolution of Ψ_A and $K\{A \Rightarrow B\}$, and compare it with Ψ_B.[12] For a perfect kernel, both quantities should coincide at all radii.

Figure 3 shows the analysis of $K\{\text{M24} \Rightarrow \text{S250}\}$.[13] This kernel shows good behavior: it transforms from a camera with $\text{FWHM}_{\text{M24}} = 6.5″$ into a camera with $\text{FWHM}_{\text{S250}} = 18.2″$. This kernel essentially spreads the energy of the core of MIPS 24 μm into a larger area. The filter f_{M24} has no effect on the construction of this kernel, because $\text{FT}(\Psi_B) \approx 0$ for $k > 0.7 \times k_{H,A}$.

The left panel of Figure 3 compares the integrated power of the PSFs. It includes Ψ_{M24} (*dot-dashed line*), Ψ_{S250} (*solid line*), and $\Psi_{\text{M24}} \star K\{\text{M24} \Rightarrow \text{S250}\}$ (*dashed line*). For an ideal kernel the solid line and the dashed line should coincide. The departures in this case are very small.

---

[12] It can be easily shown that the radial profile of $(\Psi_A \star K\{A \Rightarrow B\})$ is the same whether Ψ_A is rotationally symmetric or not, so for simplicity, we use the circularized version of Ψ_A in the comparison.

[13] In our PSF and kernel notations, we will abbreviate IRAC, MIPS, PACS, SPIRE, *GALEX*, and WISE as I, M, P, S, GAL, and W, respectively, and will omit the μm symbol.

The power per unit radius is proportional to $\theta\Psi(\theta)$, or $\theta K(\theta)$. The right panel of Figure 3 shows $\theta\Psi$ and θK (normalized to the maximum value). The lower part of the right panel includes four traces: $\theta \times \Psi_{M24}$ (*dot-dashed line*), $\theta \times \Psi_{S250}$ (*solid line*), $\theta \times (\Psi_{M24}\star K\{M24 \Rightarrow S250\})$ (*dashed line*) and $\theta \times K\{M24 \Rightarrow S250\}$ (*dotted line*) for visualization of the kernel behavior. For an ideal kernel the solid line and the dashed line should coincide. The upper part of the right panel is a plot of the difference between $\theta \times \Psi_{S250}$ and $\theta \times (\Psi_{M24}\star K\{M24 \Rightarrow S250\})$. For an ideal kernel this graph should be 0. For this example $(K\{M24 \Rightarrow S250\})$, the $\Psi_{M24}\star K\{M24 \Rightarrow S250\}$ reproduces the SPIRE 250 μm PSF to within $0.01 \times \Psi_{S250}(0)$.

In Figures 4 and 5 we analyze the kernels $K\{M70 \Rightarrow S250\}$ and $K\{S250 \Rightarrow M70\}$. Their construction is more challenging since both cameras have similar FWHM: $FWHM_{M70} = 18.7''$ and $FWHM_{S250} = 18.2''$. These kernels have to redistribute the energy within the core and Airy rings of the PSFs. The plotted quantities are similar to those in the right panel of Figure 3 for $K\{M24 \Rightarrow S250\}$. In this case, the kernels still perform well, but they have large areas with negative values.

One measure of kernel performance is its accuracy in redistribution of PSF power. We define

$$D = \iint |\Psi_B - K\{A \Rightarrow B\}\star\Psi_A|dxdy. \quad (20)$$

A kernel with perfect performance will have $D = 0$, and normalization of the PSFs requires $D \leq 2$. D measures how much flux has not been redistributed correctly. Good kernels have small D values: $D(K\{M24 \Rightarrow S250\}) = 0.011$. In Table 4 we give D for the kernels constructed.
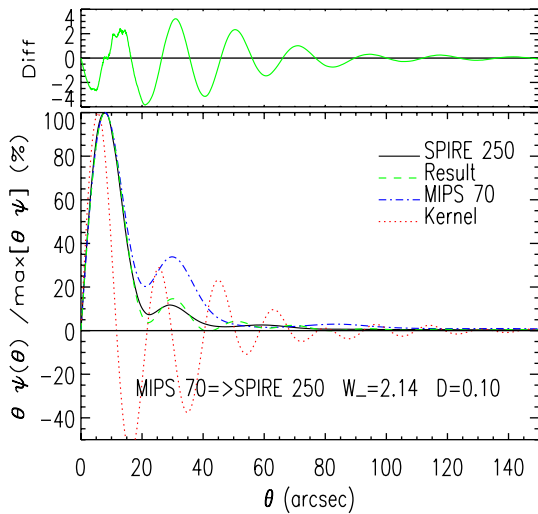
A second quantitative measure of kernel performance is obtained by studying its negative values. We define

$$W_{\pm} = \frac{1}{2}\iint (|K\{A \Rightarrow B\}| \pm K\{A \Rightarrow B\})dxdy. \quad (21)$$

Flux conservation requires that $W_+ = 1 + W_-$. In general, kernels will have $W_- > 0$. Well-behaved kernels have small W_- values: $W_-(K\{M24 \Rightarrow SP250\}) = 0.07$. The integral of $|K\{A \Rightarrow B\}|$ is $[1 + 2W_-]$, so a kernel with a large value of W_- could potentially amplify image artifacts. Additionally, a kernel with large W_- can generate areas of negative flux near point sources if nonlinearities are present or if the background levels were subtracted incorrectly. Table 5 lists the W_- values for the kernels constructed. The values in Table 5 were computed numerically. Due to finite grid resolution the numerical values may be off by a few percent in some cases. This can be seen from the W_- values computed for the self-kernels. The self-kernels are simply the Fourier transform of the filter f_A, and W_- should therefore be the same (1.15) in all cases. However, in Table 5 the W_- for the smallest PSFs are larger than 1.15 by as much as 0.03 (e.g., 1.18 for PACS 70 μm).

Essentially, there are two sources of W_-: oscillations due to the filter f_A and the need to remove energy from some region to relocate to another region (when the target Ψ_B is narrower than Ψ_A or has less energy in some annuli).

The kernels between cameras with similar FWHM also have oscillations. Using a softer filter f_A would reduce the oscillatory

FIG. 4.—Performance of the kernel $K\{M70 \Rightarrow S250\}$. Because of the large value $W_- = 2.14$, convolution MIPS70 μm $\Rightarrow$ SPIRE250 μm is not recommended. See the electronic edition of the *PASP* for a color version of this figure.

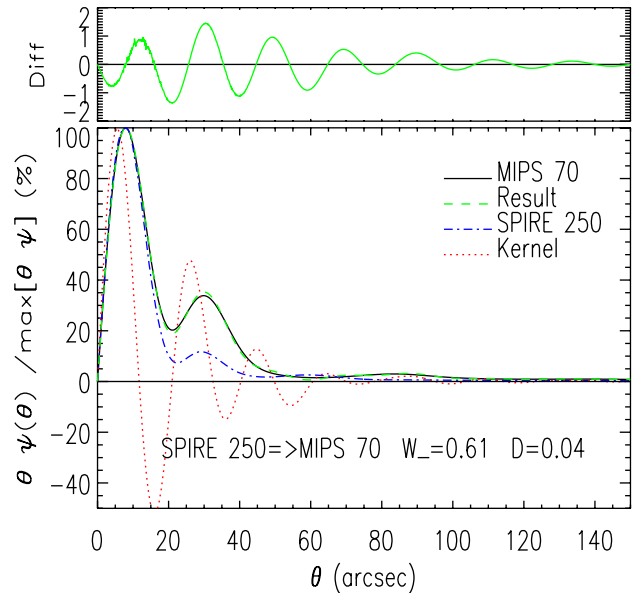FIG. 5.—Performance of the kernel $K\{S250 \Rightarrow M70\}$. With $W_- = 0.61$, this kernel is safe to use. $\Psi_{S250}\star K\{S250 \Rightarrow M70\}$ deviates from Ψ_{M70} less than 2%. See the electronic edition of the *PASP* for a color version of this figure.

TABLE 4
D VALUES FOR CONSTRUCTED KERNELS

From	To														
	M 24	M 70	M 160	P 70	P 100	P 160	S 250	S 350	S 500	GAL FUV	GAL NUV	W 3.4	W 4.6	W 11.6	W 22.1
I3.6	0.065	0.029	0.037	0.051	0.047	0.031	0.025	0.022	0.018	0.006	0.005	0.005	0.005	0.007	0.008
I4.5	0.065	0.029	0.037	0.051	0.047	0.031	0.025	0.022	0.018	0.006	0.005	0.005	0.005	0.007	0.008
I5.8	0.064	0.031	0.048	0.047	0.045	0.031	0.029	0.027	0.018	0.012	0.010	0.012	0.012	0.013	0.012
I8.0	0.064	0.030	0.047	0.047	0.046	0.032	0.026	0.024	0.018	0.012	0.007	0.007	0.007	0.009	0.009
M24	0.091	0.018	0.048	0.213	0.068	0.015	0.011	0.013	0.017	NC	0.352	0.225	0.122	0.098	0.027
M70	NC	0.055	0.038	NC	NC	NC	0.102	0.015	0.014	NC	NC	NC	NC	NC	NC
M160	NC	NC	0.064	NC	NC	NC	NC	NC	0.169	NC	NC	NC	NC	NC	NC
P70	0.006	0.019	0.049	0.045	0.010	0.014	0.011	0.014	0.017	0.227	0.113	0.064	0.045	0.027	0.027
P100	0.072	0.014	0.045	0.188	0.050	0.010	0.011	0.014	0.015	NC	NC	0.202	0.111	0.087	0.028
P160	NC	0.009	0.040	NC	NC	0.044	0.013	0.014	0.015	NC	NC	NC	NC	NC	0.032
S250	NC	0.037	0.045	NC	NC	NC	0.058	0.009	0.014	NC	NC	NC	NC	NC	NC
S350	NC	0.300	0.043	NC	NC	NC	NC	0.060	0.012	NC	NC	NC	NC	NC	NC
S500	NC	NC	0.042	NC	NC	NC	NC	NC	0.055	NC	NC	NC	NC	NC	NC
FUV	0.065	0.030	0.036	0.049	0.046	0.032	0.025	0.024	0.018	0.046	0.017	0.007	0.006	0.007	0.007
NUV	0.065	0.030	0.037	0.051	0.046	0.032	0.027	0.024	0.018	0.071	0.028	0.008	0.006	0.006	0.007
W 3.4	0.066	0.029	0.037	0.080	0.048	0.032	0.026	0.023	0.018	0.252	0.122	0.053	0.034	0.017	0.007
W 4.6	0.066	0.029	0.037	0.079	0.047	0.032	0.026	0.023	0.018	NC	0.118	0.051	0.033	0.016	0.006
W 11.6	0.074	0.028	0.037	0.117	0.056	0.031	0.026	0.023	0.018	NC	0.206	0.109	0.063	0.040	0.005
W 22.1	NC	0.028	0.036	NC	NC	0.163	0.028	0.023	0.018	NC	NC	NC	NC	NC	0.094

NOTES.—D is the integral of the absolute value of the difference between a target PSF and the PSF reproduced by the kernel (see eq. [20]). We are abbreviating IRAC, MIPS, PACS, SPIRE, *GALEX*, and WISE as I, M, P, S, GAL, and W, respectively. NC stands for not computed: the kernel performance would be too poor.

TABLE 5
W_- VALUES FOR CONSTRUCTED KERNELS

From		M 24	M 70	MI 160	P 70	P 100	P 160	S 250	S 350	S 500	GAL FUV	GAL NUV	W 3.4	W 4.6	W 11.6	W 22.1
I3.6	....	0.00	0.00	0.00	0.00	0.00	0.00	0.00	0.00	0.00	0.06	0.03	0.05	0.05	0.05	0.02
I4.5	....	0.01	0.00	0.00	0.00	0.00	0.00	0.00	0.00	0.00	0.07	0.03	0.05	0.05	0.05	0.02
I5.8	....	0.15	0.03	0.02	0.07	0.07	0.03	0.05	0.05	0.02	0.29	0.23	0.25	0.24	0.23	0.15
I8.0	....	0.11	0.00	0.00	0.01	0.01	0.00	0.00	0.01	0.00	0.23	0.11	0.14	0.14	0.12	0.06
M24	....	1.17	0.02	0.00	2.85	0.75	0.16	0.06	0.04	0.01	NC	5.14	3.28	1.83	1.11	0.32
M70	....	NC	1.15	0.20	NC	NC	NC	2.14	0.66	0.34	NC	NC	NC	NC	NC	NC
M160	....	NC	NC	1.14	NC	NC	NC	NC	NC	2.81	NC	NC	NC	NC	NC	NC
P70	....	0.83	0.01	0.01	1.18	0.32	0.00	0.05	0.05	0.02	5.74	2.68	1.48	0.77	0.48	0.16
P100	....	2.16	0.01	0.01	4.29	1.17	0.04	0.07	0.06	0.03	NC	NC	4.82	2.56	1.75	0.24
P160	....	NC	0.11	0.02	NC	NC	1.16	0.24	0.14	0.06	NC	NC	NC	NC	NC	1.10
S250	....	NC	0.61	0.02	NC	NC	NC	1.15	0.21	0.06	NC	NC	NC	NC	NC	NC
S350	....	NC	6.08	0.08	NC	NC	NC	NC	1.15	0.14	NC	NC	NC	NC	NC	NC
S500	....	NC	NC	0.47	NC	NC	NC	NC	NC	1.14	NC	NC	NC	NC	NC	NC
FUV	....	0.15	0.00	0.00	0.10	0.01	0.00	0.00	0.00	0.00	1.18	0.30	0.21	0.11	0.07	0.03
NUV	....	0.33	0.00	0.00	0.47	0.07	0.00	0.00	0.00	0.00	3.35	1.18	0.60	0.26	0.12	0.03
W 3.4	....	0.60	0.00	0.00	1.05	0.21	0.00	0.01	0.00	0.00	5.02	2.37	1.18	0.53	0.29	0.01
W 4.6	....	1.27	0.00	0.00	2.19	0.56	0.00	0.01	0.00	0.00	NC	4.29	2.43	1.18	0.83	0.04
W 11.6	....	2.06	0.02	0.00	3.14	1.14	0.22	0.07	0.02	0.00	NC	5.70	3.52	1.95	1.17	0.35
W 22.1	....	NC	0.39	0.01	NC	NC	1.65	0.60	0.28	0.04	NC	NC	NC	NC	NC	1.16

NOTES.—W_- is the integral of the negative values for each kernel (see eq. [21]).
We are abbreviating IRAC, MIPS, PACS, SPIRE, *GALEX*, and WISE as I, M, P, S, GAL, and W, respectively. NC stands for not computed: the kernel performance would be too poor.
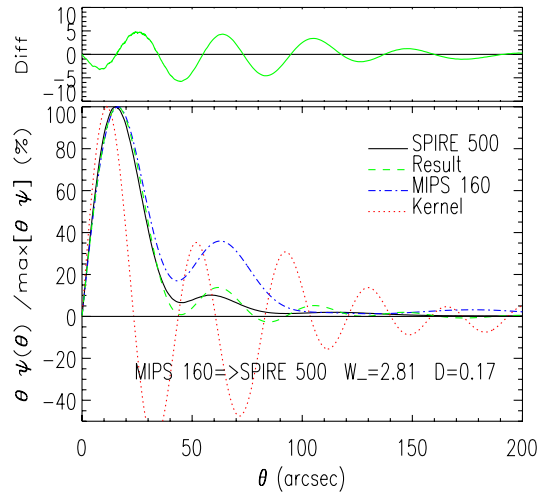
FIG. 6.—Performance of the kernel $K\{M160 \Rightarrow S500\}$. With $W_- = 2.81$, convolution of MIPS 160 μm images into SPIRE 500 μm resolution is risky and not recommended. The convolved PSF differs from the target PSF by up to 6%. See the electronic edition of the *PASP* for a color version of this figure.
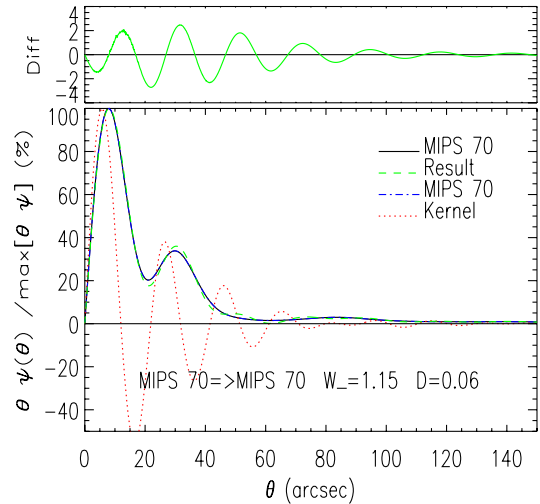

FIG. 7.—Performance of the self-kernel $K\{M70 \Rightarrow M70\}$. All of the self-kernels have $W_- = 1.16$ and reproduce the original PSF to within 3%. See the electronic edition of the *PASP* for a color version of this figure.

behavior, giving smaller values of W_-, but would also produce worse matched PSFs (larger values of D). The particular form of filter f_A used in the present work is a good compromise between having good PSF matching and moderate oscillatory behavior.

In Figure 6 we analyze a kernel of particular interest: $K\{M160 \Rightarrow S500\}$. Despite both cameras having similar FWHM (FWHM$_{M160}$/FWHM$_{S500}$ = 1.07), their extended wings are very different. The kernel $K\{M160 \Rightarrow S500\}$ is particularly badly behaved, with large negative excursions, having $W_- = 2.81$ and $D = 0.17$. In a convolution of MIPS 160 μm images of NGC 6946, some bright point sources generated regions with negative flux around them. We do not recommend using the kernel $K\{M160 \Rightarrow S500\}$; if MIPS 160 μm and SPIRE 500 μm images need to be combined, we recommend

using the PSF of MIPS 160 μm ($K\{S500 \Rightarrow M160\}$ has $W_- \approx 0.47$ and $D \approx 0.042$) or some Gaussian PSF compatible with MIPS 160 μm, such as a Gaussian with FWHM = $64''$ (see § 6).

Finally, in Figure 7 we analyze the kernel $K\{M70 \Rightarrow M70\}$. This kernel is essentially FT(f_{M70}), and it illustrates the effect of all the kernel construction steps. All the kernels of the form $K\{A \Rightarrow A\}$ are scaled versions of $K\{M70 \Rightarrow M70\}$, aside from small differences due to finite grids. All of the $K\{A \Rightarrow A\}$ kernels have $W_- \approx 1.15$ and $D \approx 0.06$.

Even though kernels $K\{A \Rightarrow A\}$ have $W_- = 1.15$ and $W_+ = 2.15$, they do not amplify the noise that arises from astronomical sources. The image of an astronomical point source will be Ψ_A. When we convolve the camera with a kernel of the form $K\{A \Rightarrow A\}$, the image of a point source will still be very close to Ψ_A, since $D(K\{A \Rightarrow A\}) \sim 0.06$. This implies that the

TABLE 6
GAUSSIAN FWHM SUITABLE FOR MIPS, PACS, AND SPIRE CAMERAS

| Camera	Actual FWHM (″)	Aggressive Gaussian with $W_- \approx 1.0$		Moderate Gaussian with $W_- \approx 0.5$		Very safe Gaussian with $W_- \approx 0.3$	
		FWHM (″)	W_-	FWHM (″)	W_-	FWHM (″)	W_-
MIPS 24 μm	6.5	8.0	1.00	11.0	0.49	13.0	0.30
MIPS 70 μm	18.7	22.0	1.01	30.0	0.51	37.0	0.30
MIPS 160 μm	38.8	46.0	1.01	64.0	0.50	76.0	0.30
PACS 70 μm	5.8	6.5	0.84	8.0	0.48	10.5	0.31
PACS 100 μm	7.1	7.5	1.10	9.0	0.52	12.5	0.31
PACS 160 μm	11.2	12.0	1.05	14	0.50	18.0	0.33
SPIRE 250 μm	18.2	19.0	1.05	21.0	0.44	22.0	0.30
SPIRE 350 μm	25.0	26.0	0.98	28.0	0.50	30.0	0.27
SPIRE 500 μm	36.4	38.0	0.96	41.0	0.48	43.0	0.30
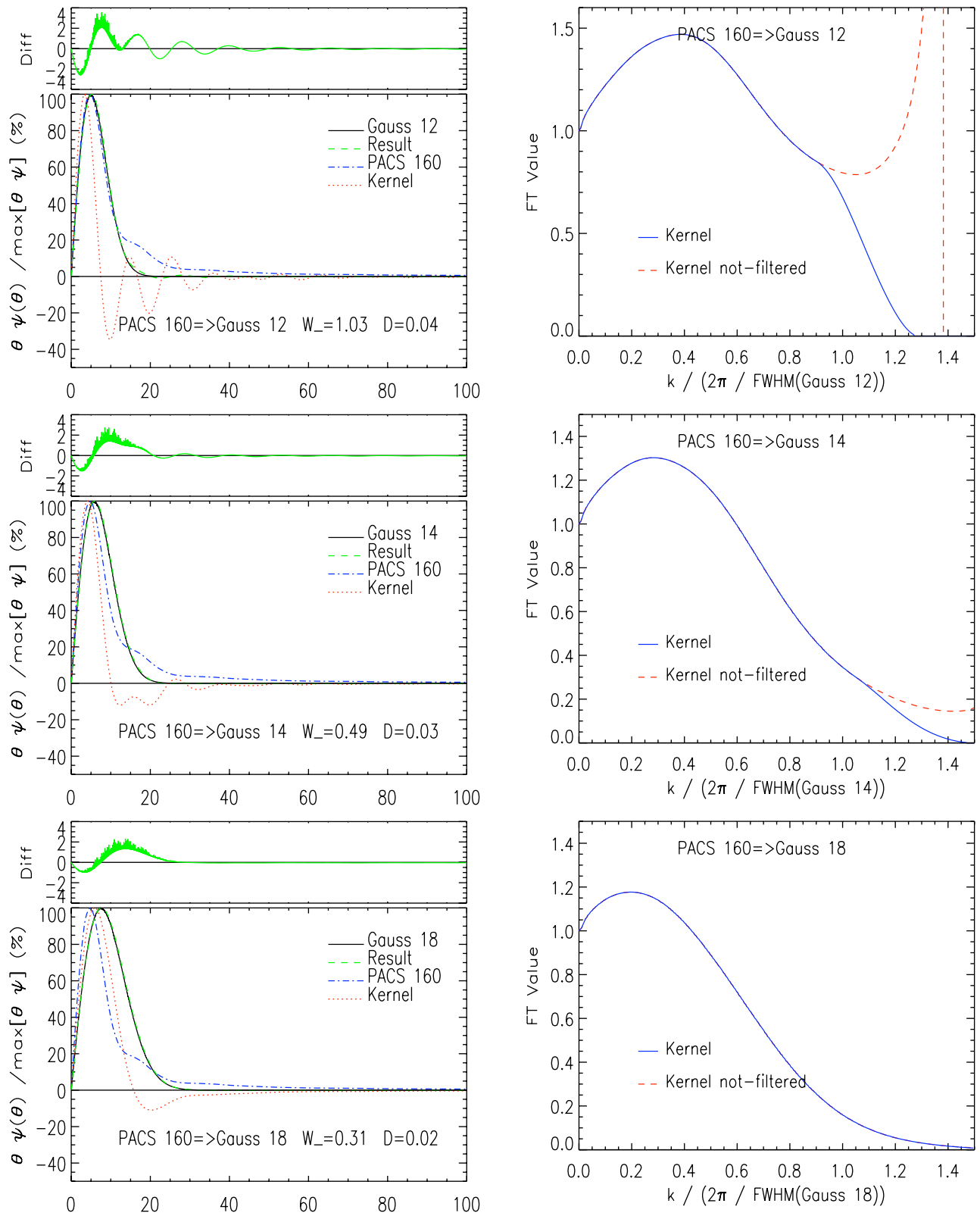
FIG. 8.—Performance of the kernels $K\{P160 \Rightarrow \text{Gaussian}\}$ (*left*) and their FT (*right*). We show the kernel Fourier transform $\text{FT}(K)$ (eq. [19]) and also the unfiltered kernel Fourier transform [$=\text{FT}_\phi(\Psi_B)/\text{FT}_\phi(\Psi_A)$]. The filter f_{P160} has little impact on $K\{P160 \Rightarrow \text{Gaussian}18''\}$ ($W_- = 0.33$), moderate effect on $K\{P160 \Rightarrow \text{Gaussian}14''\}$ ($W_- = 0.50$), and large effect on $K\{P160 \Rightarrow \text{Gaussian}12''\}$ ($W_- = 1.05$). See the electronic edition of the *PASP* for a color version of this figure.
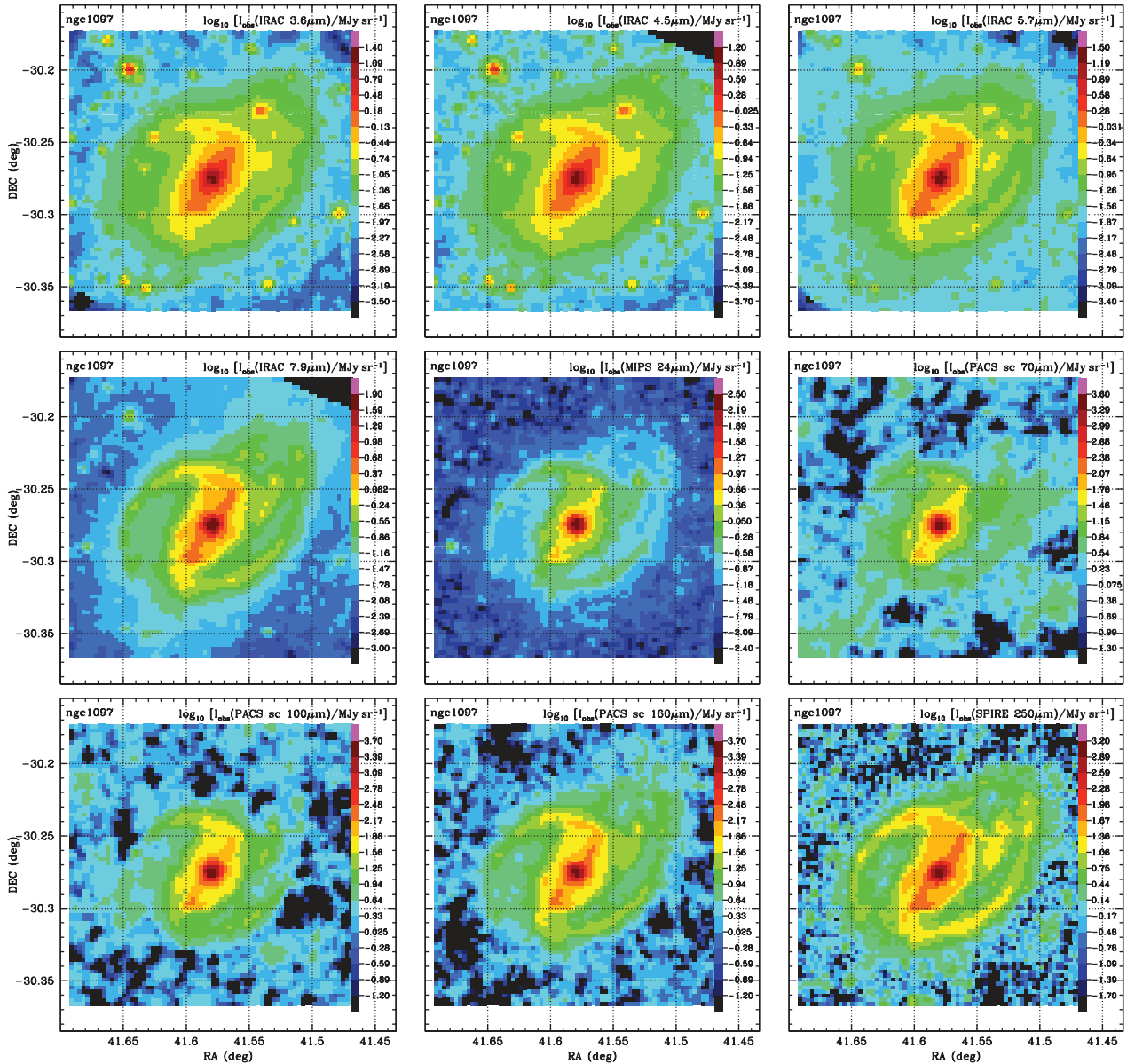
FIG. 9.—*Spitzer* and *Herschel* images of NGC 1097 convolved to a SPIRE 250 μm PSF. The SPIRE 250 μm camera was convolved with the kernel $K\{S250 \Rightarrow S250\}$. The color bar has the same dynamic range $(10^{4.9})$ for all images

noise coming from a field of unresolved astronomical background sources will not change significantly when we convolve the image with $K\{A \Rightarrow A\}$. To verify this reasoning, we generate an image S having independent Gaussian noise in each pixel in a very fine (0.2″) grid. We convolve S with Ψ_{M70} to have a simulated observed image of the noise: $O = S \star \Psi_{M70}$. We further convolve O with $K\{M70 \Rightarrow M70\}$: $C = O \star K\{M70 \Rightarrow M70\}$. We found that $|1 - \langle C^2 \rangle / \langle O^2 \rangle| \approx 10^{-3}$. While uncorrelated noise is not amplified by a self-kernel $K\{A \Rightarrow A\}$, imprecise characterization of the PSFs and

camera artifacts can be amplified by kernels with large W_- values.

There is no single number that captures all of the characteristics of a convolution kernel, but we find that W_- serves as a good figure of merit. Based on experimentation with various kernels, we regard kernels with $W_- \lesssim 0.3$ to be very safe. Kernels with $W_- \approx 0.5$ also appear to be quite safe. A kernel with $W_- \approx 1$ is somewhat aggressive in moving power around, but remember that self-kernels $K\{A \Rightarrow A\}$ also have $W_- \approx 1.15$. We consider kernels with $W_- \approx 1$ to be reasonable
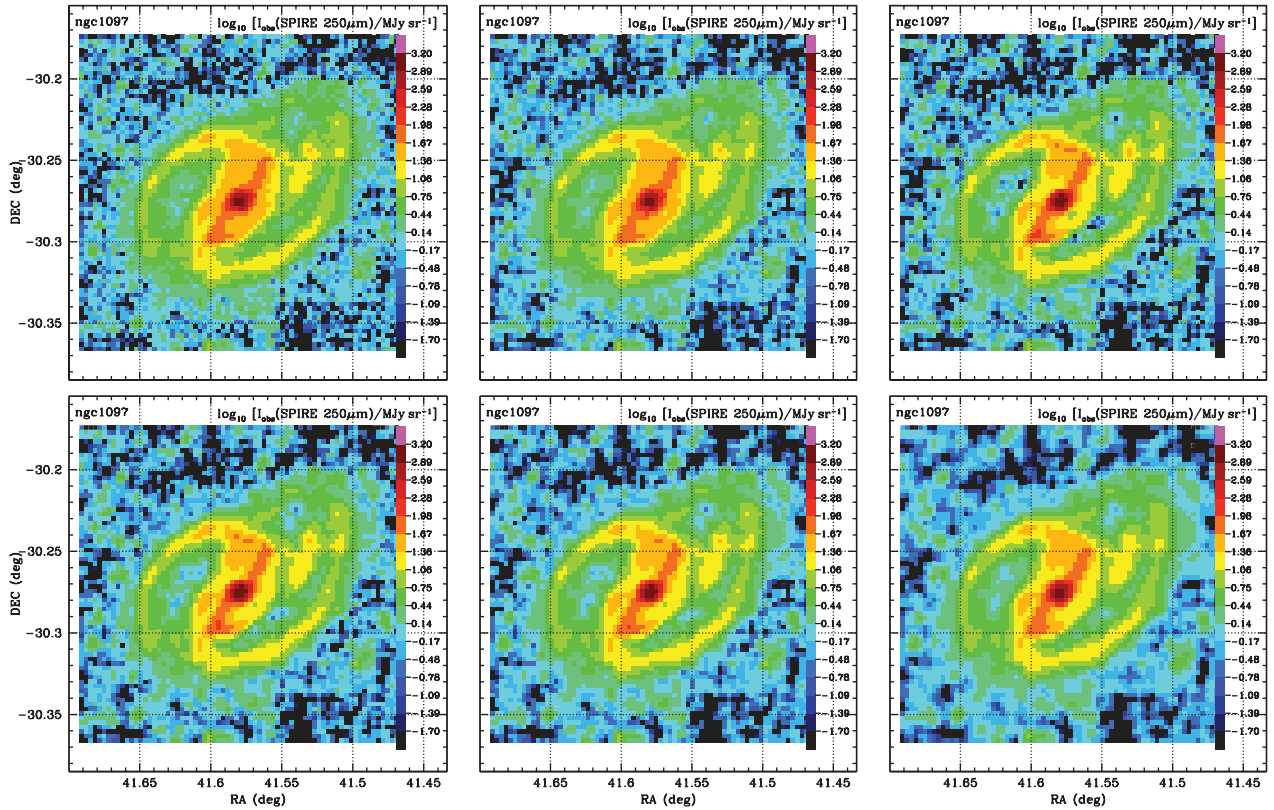
F𝚒ɢ. 10.—SPIRE 250 μm image of NGC 1097. *Top left*: Original SPIRE image. *Top middle*: Image convolved with $K\{S250 \Rightarrow S250\}$. *Top right*: image convolved into an extremely aggressive convolution to a Gaussian PSF with FWHM = 18″ ($W_- = 1.47$). *Bottom*: Image convolved with suitable Gaussian PSFs. *Bottom left*: (aggressive) FWHM = 19″ ($W_- = 1.05$). *Bottom middle*: (moderate) FWHM = 21″ ($W_- = 0.44$). *Bottom right*: (very safe) FWHM = 22″ ($W_- = 0.30$). All the images have the same color bar.

to use, with inspection of the before and after images recommended in regions with large gradients or bright sources. We recommend against using convolution kernels with $W_- > 1.2$, as these are, in effect, attempts to deconvolve the image to higher resolution, with attendant risks.

6. GAUSSIAN PSFs

Gaussian PSFs are commonly used in radio astronomy. It is desirable for radio telescopes to have PSFs without extended structure to avoid sidelobe contamination. The illumination pattern of a single dish is often designed to return an approximately Gaussian PSF.[14] A Gaussian PSF lacks extended wings; the fraction of the power outside radius θ is $\exp(-\theta^2/2\sigma^2)$. Because real instrumental PSFs do not fall off so rapidly, a convolution kernel K going from a real Ψ_A to a Gaussian Ψ_B with similar FWHM must "move" power from the wings of Ψ_A to the core of Ψ_B.

For a given instrumental PSF Ψ_A, the optimal Gaussian PSF Ψ_B will be such that the FWHM_B will be close to FWHM_A, with only mild filtering by the function f_A and with W_- not too large.

In order to determine an optimal Gaussian FWHM for a camera A, we compute convolution kernels from A into Gaussian PSFs with FWHM in a range of possible values. For each candidate FWHM, we evaluate W_-. We provide three possible FWHM. The first FWHM is obtained by requiring that $W_- \sim 0.3$, giving a conservative (very safe) kernel that does not seek to move too much energy from the wings into the main Gaussian core, at the cost of having a larger FWHM (i.e., lower resolution). The second FWHM has $W_- \sim 0.5$, and we consider it to be a good (moderate) Gaussian FWHM to use. The third FWHM has $W_- \sim 1.0$. Because this kernel is somewhat "aggressive" in moving energy from the PSF wings into the Gaussian core, it should be used with care, inspecting that the convolved images do not have any induced artifact. Table 6 gives the FWHM for three such Gaussian target PSFs for the MIPS, PACS, and SPIRE cameras.

As an example, Figure 8 shows the performance of the kernels for the PACS 160 μm camera going into Gaussian

---

[14] Interferometric arrays have complicated sidelobe responses and would not resemble Gaussian PSFs.

PSFs with FWHM $= 12''$ (aggressive, $W_- = 1.05$ $D = 0.05$), $14''$ (moderate, $W_- = 0.50$, $D = 0.02$), and $18''$ (very safe, $W_- = 0.33$, $D = 0.01$). The left panels are the performance analyses, similar to those of Figures 47. The right panels show the kernel Fourier transform $\mathrm{FT}(K)$ (eq. [19]. In the right panel, we include the unfiltered Fourier transform $(= \mathrm{FT}_\phi(\Psi_{\mathrm{Gauss}}) / \mathrm{FT}_\phi(\Psi_{\mathrm{P160}}))$ for comparison (*dotted line*). We observe that the filtering is only important in the Gaussian kernels with (small) FWHM $= 12''$ and $14''$.

7. USAGE OF THE KERNELS

The kernels $K\{A \Rightarrow B\}$ computed here are given on a $0.20''$ grid. Before performing an image convolution, the kernel $K\{A \Rightarrow B\}$ should be resampled onto a grid with the same pixel size as the original image I_A. The resampled kernels should be centered (to avoid shifts in the image) and normalized so that $\iint K\{A \Rightarrow B\}(x, y)dxdy = 1$ to ensure flux conservation. The flux in the image to be convolved should be in surface brightness units. After convolving the image I_A with the kernel $K\{A \Rightarrow B\}$, the resulting image will be expressed in the original image grid and original surface brightness units, but with PSF Ψ_B.

Table 5 also summarizes the kernels available. For each camera A we construct all the kernels $K\{A \Rightarrow B\}$ with $\mathrm{FWHM}_B \geq \mathrm{FWHM}_A/1.35$ (i.e., the kernels that degrade the resolution or sharpen it up to 35%) plus the self-kernels $K_{A \Rightarrow A}$. Kernels with $\mathrm{FWHM}_A \gtrsim \mathrm{FWHM}_B$ (that have larger W_- values) tend to perform poorly and should be used with care. We do not recommend using any kernel with $W_- \gtrsim 1.2$.

As an example of the performance of the kernels applied to real (noisy) images, in Figure 9 we show the result of convolving images of the barred spiral galaxy NGC 1097 (after subtraction of a "tilted-plane" background from each image) into the SPIRE 250 μm PSF. The PACS images have been reduced using the Scanamorphos pipeline (Roussel 2011). Visual inspection of the images in Figure 9 shows them to be very similar in morphology; the convolution does not appear to have introduced any noticeable artifact.

Figure 10 shows the results of convolving the SPIRE 250 μm image into different PSFs. The top row (*left*) shows the original[15] image, (*center*) the image convolved with $K\{\mathrm{S250} \Rightarrow \mathrm{S250}\}$, and (*right*) the image convolved with a very aggressive kernel into a Gaussian PSF with FWHM $= 18''$ ($W_- = 1.47$). The bottom row shows the image convolved to the recommended Gaussian PSFs: (*left*) FWHM $= 19''$ ($W_- = 1.05$), (*center*) FWHM $= 21''$ ($W_- = 0.44$), and (*right*) FWHM $= 22''$ ($W_- = 0.30$).

As discussed in § 5, we recommend against using kernels with $W_- > 1.2$. Visual inspection of the upper-right image in fact shows artifacts where the kernel (with $W_- = 1.47$) has moved too much power out of some interarm pixels, which have been brought down to unreasonably low intensities. In the convolutions to the suitable Gaussian PSFs (*bottom row* in Fig. 10) energy is moved from the interarm regions into the bright nucleus and spiral arms, but the intensity levels in the interarm regions seem reasonable. The power that is removed from the interarm regions was presumably originally power from the arms that was transferred by the wings of the SPIRE 250 μm PSF.

Using the kernels described in the current work, Aniano et al. (2011, in preparation) studied resolved dust modeling for NGC 628 and NGC 6946, two galaxies in the KINGFISH galaxy sample (Kennicutt et al. 2011, in preparation), using images obtained with *Spitzer* and *Herschel Space Observatory*.

8. SUMMARY

We present the construction and analysis of convolution kernels for transforming images into a common PSF. They allow generation of a multiwavelength image cube with a common PSF, preserving the colors of the regions imaged.

We generate and make available a library of convolution kernels for the cameras of *Spitzer*, *Herschel Space Observatory*, *GALEX*, WISE, ground-based telescopes, and Gaussian PSFs. All the kernels are constructed with the best PSF characterizations available, approximated by rotationally symmetric functions. Deviations of the actual PSF from circular symmetry are characterized by an asymmetry parameter g, given in Table 1. Table 5 summarizes the kernels available and their negative integral W_-, a measure of their performance. We recommend using only kernels with $W_- \lesssim 1.2$. In Table 6 we give a set of optimal Gaussian FWHM that are compatible with MIPS, PACS, and SPIRE cameras.

All the kernels and their individual performance analyses, the IDL routines to make new kernels, and IDL routines to use them are publicly available.[16]

---

[15] By "original" image we refer to the SPIRE 250 μm image delivered by the HIPE pipeline, with subsequent subtraction of a tilted-plane background. This is the original image that is convolved to produce the other images in Fig. 10.

[16] See http://www.astro.princeton.edu/~draine/Kernels.html. Kernels for additional cameras and updates will be included when new PSF characterizations become available.

REFERENCES

Alard, C., & Lupton, R. H. 1998, ApJ, 503, 325

Engelbracht, C. W., et al. 2007, PASP, 119, 994

Fazio, G. G., et al. 2004, ApJS, 154, 10

Geis, N., & Lutz, D. 2010, PACS ICC Document, PICC-ME-TN-029 v2.0

Gordon, K. D., Engelbracht, C. W., Rieke, G. H., Misselt, K. A., Smith, J., & Kennicutt, R. C., Jr. 2008, ApJ, 682, 336

Gordon, K. D., et al. 2007, PASP, 119, 1019

Griffin, M. J., et al. 2010, A&A, 518, L3

Lutz, D. 2010, PACS ICC Document, PICC-ME-TN-033

Martin, D. C., et al. 2005, ApJ, 619, L1

Moffat, A. F. J. 1969, A&A, 3, 455

Müller, T. 2010, PACS ICC Document, PICC-ME-TN-036 v2.0

Poglitsch, A., et al. 2010, A&A, 518, L2

Racine, R. 1996, PASP, 108, 699

Rieke, G. H., et al. 2004, ApJS, 154, 25

Roussel, H. 2011, A&A, submitted

Sandstrom, K. M., Bolatto, A. D., Stanimirović, S., van Loon, J. T., & Smith, J. D. T. 2009, ApJ, 696, 2138

Stansberry, J. A., et al. 2007, PASP, 119, 1038

Wright, E. L., et al. 2010, AJ, 140, 1868